Geophysical Prospecting, 2003, **51**, 501–515

Seismic modelling study of a subglacial lake

José M. Carcione* and Davide Gei

Istituto Nazionale di Oceanografia e di Geofisica Sperimentale (OGS), Borgo Grotta Gigante 42C, 34010 Sgonico, Trieste, Italy

Received January 2002, revision accepted June 2003

ABSTRACT

We characterize the seismic response of Lake Vostok, an Antarctic subglacial lake located at nearly 4 km depth below the ice sheet. This study is relevant for the determination of the location and morphology of subglacial lakes. The characterization requires the design of a methodology based on rock physics and numerical modelling of wave propagation. The methodology involves rock-physics models of the shallow layer (firn), the ice sheet and the lake sediments, numerical simulation of synthetic seismograms, ray tracing, τ–p transforms, and AVA analysis, based on the theoretical reflection coefficients. The modelled reflection seismograms show a set of straight events (refractions through the firn and top-ice layer) and the two reflection events associated with the top and bottom of the lake. Theoretical AVA analysis of these reflections indicates that, at near offsets, the PP-wave anomaly is negative for the ice/water interface and constant for the water/sediment interface. This behaviour is shown by AVA analysis of the synthetic data set. This study shows that subglacial lakes can be identified by using seismic methods. Moreover, the methodology provides a tool for designing suitable seismic surveys.

INTRODUCTION

Lake Vostok is located in East Antarctica between 76.2°S/102°E and 78.4°S/108°E (extending about 230 km to the north of the Vostok station), beneath nearly 4 km of glacial ice (Fig. 1). This lake, believed to be the largest subglacial lake, has been surveyed by airborne 60 MHz radio-echo soundings (Robin, Drewry and Meldrum 1977; Ridley, Cudlip and Laxon 1993; Kapitsa *et al.* 1996) and seismic surveys (Kapitsa *et al.* 1996; Masolov *et al.* 1999). An indirect indication of these lakes is the flat surface above the ice sheet. A review of Antarctic subglacial lakes, and in particular, an analysis of the ice-sheet features above Lake Vostok, is given in Siegert and Ridley (1998) and Siegert (2000). Lake Vostok, nearly 14 000 km^2 in area, is comparable in size with that of Lake Ontario. Its meltwater age is estimated to be tens of thousands of years, and its mean age, since deposition as surface ice, is approximately one million years. Hence, one of the outstanding facts related to Lake Vostok is that this lake provides an opportunity to study a lake system that has been isolated from the earth's atmosphere through most of the Pleistocene and Holocene.

The use of seismic methods is one possibility of determining the location and morphology of subglacial lakes. Kapitsa *et al.* (1996) analysed and detected reflection events corresponding to the ice/water interface and the water/sediment interface at nearly 1.9 s and 2.6 s two-way traveltimes, respectively. These seismic data were acquired by Kapitsa and Sorochtin in 1964 (see Kapitsa *et al.* 1996), using vertical seismometers spread from 2.5 m to 49 m depth (24 channels) in a borehole located 180 m away from an explosive source. This vertical seismic profile (VSP) survey, performed 1 km northwest of the Vostok station, indicated a lake depth of approximately 500 m.

A borehole was drilled, starting in 1989 and completed during the 1997–98 field season. Ice coring reached 3623 m depth, and drilling stopped 120 m above the ice/water interface to prevent contamination of the lake by kerosene-based drilling fluid (Petit 1998). In this borehole, Masolov *et al.* (1999) recorded a VSP down to 3615 m depth. Explosive sources (1.5–2 kg) were positioned in shallow holes (2.5 m depth)

*E-mail: jcarcione@ogs.trieste.it

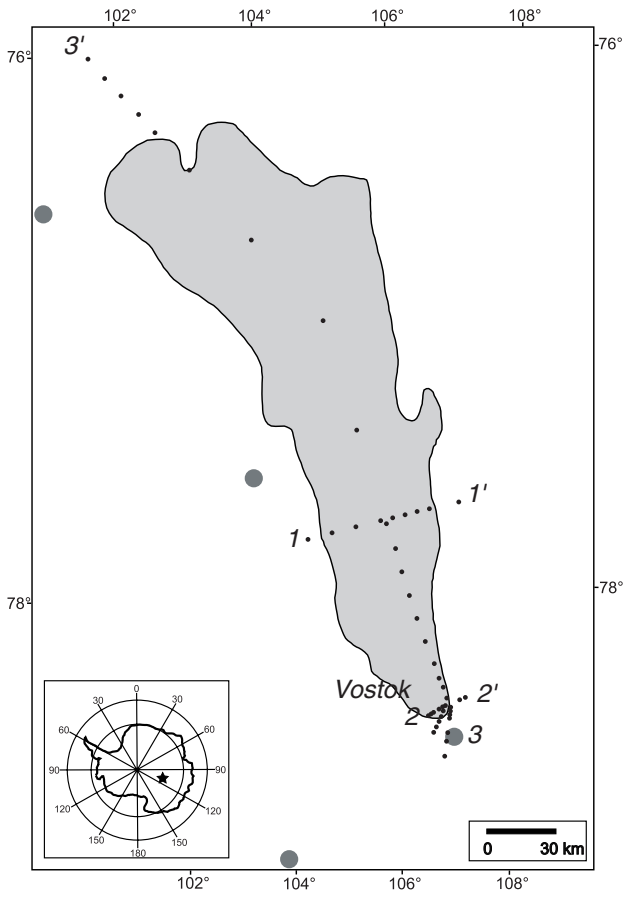

Figure 1 Lake Vostok is located in East Antarctica, beneath nearly 4 km of glacial ice. The dots indicate the location of the seismic data acquired in the area (see Masolov *et al.* (1999) for more details).

for recording intervals of 200 m between 300 and 2600 m depth, and in deeper holes (150 m, below the firn layer) for recording intervals of 25–50 m below 2600 m depth. (The source–borehole distance is 100 m approximately.) In addition, 80 common-shot gathers were acquired with 24-channel arrays, 600–1200 m long with 25–50 m spacing between geophone arrays. The nearest offset ranged from 3.5 to 11 km, and the source was explosive cord. The seismograms (see Fig. 2) show clear evidence of the ice/water interface, the lake floor and the basement top. On the basis of this information, the estimated sediment thickness ranges from tens of metres to 350 m.

There is a need for suitable models for studying the seismic response of subglacial lakes and planning seismic reflection surveys. In this work, we study the seismic visibility of the lake using seismic modelling and analyse the amplitude variations with angle (AVA) characteristics of the ice/water and water/sediment interfaces by computing the corresponding reflection and refraction coefficients. The geological model is defined by using available seismic information and poroelastic models that take into account the *in situ* conditions of the different layers versus temperature and pressure. This study is undertaken to analyse Lake Vostok data with the purpose of designing an optimal seismic survey, and also to provide a general procedure for modelling the seismic response of subglacial lakes.

The paper is organized as follows. Firstly, we design the Lake Vostok seismic model by using poroelasticity and viscoelasticity theories. Next, the reflection coefficients of the main interfaces are analysed. Finally, we define the numerical-modelling equations and obtain a complete surface seismic survey and vertical seismic profile. We process these synthetic seismograms to estimate the AVA response of the ice/water interface. The aim of our analysis is to show the main features associated with the seismic response of a typical subglacial lake.

LAKE VOSTOK SEISMIC MODEL

The seismic model of Lake Vostok is shown in Fig. 3 and Table 1. The information was obtained from Kapitsa *et al.* (1996) and Masolov *et al.* (1999), who provided a P-wave velocity profile derived from a VSP at the Vostok station borehole. The seismic properties of the different layers and water are obtained by using poroelastic and viscoelastic models, that take into account the pressure–temperature conditions (see Appendix A). The determination of these seismic properties is described below.

The density of polar air at atmospheric conditions is obtained from the van der Waals equation (A5) and the bulk modulus is given by equation (A8). We obtain $\rho_a = 1.61$ kg/m^3 and $K_a = 0.135$ MPa. These values yield a sound velocity of 289 m/s (compared with 324 m/s at 0°C).

Pure ice is transversely isotropic. We calculate its properties at atmospheric conditions in the Lake Vostok area ($T = -55$°C, $p = 0.1$ MPa) using equations given in Appendix A.4 and Table 2 (Angenheister 1982). We obtain

$$\begin{aligned} c_{11} &= 15.21\,\text{GPa}, \quad c_{13} = 6.20\,\text{GPa}, \\ c_{33} &= 13.88\,\text{GPa}, \quad c_{55} = 3.03\,\text{GPa}, \end{aligned} \tag{1}$$

which implies a vertical P-wave velocity $V_P = 3886$ m/s associated with c_{33} and a shear-wave velocity $V_S = 1816$ m/s from c_{55} (see also Thiel and Ostenso (1961) for more information about the elasticity constants of ice). We do not consider here the elastic constants c_{12} and c_{66}, which are associated with the

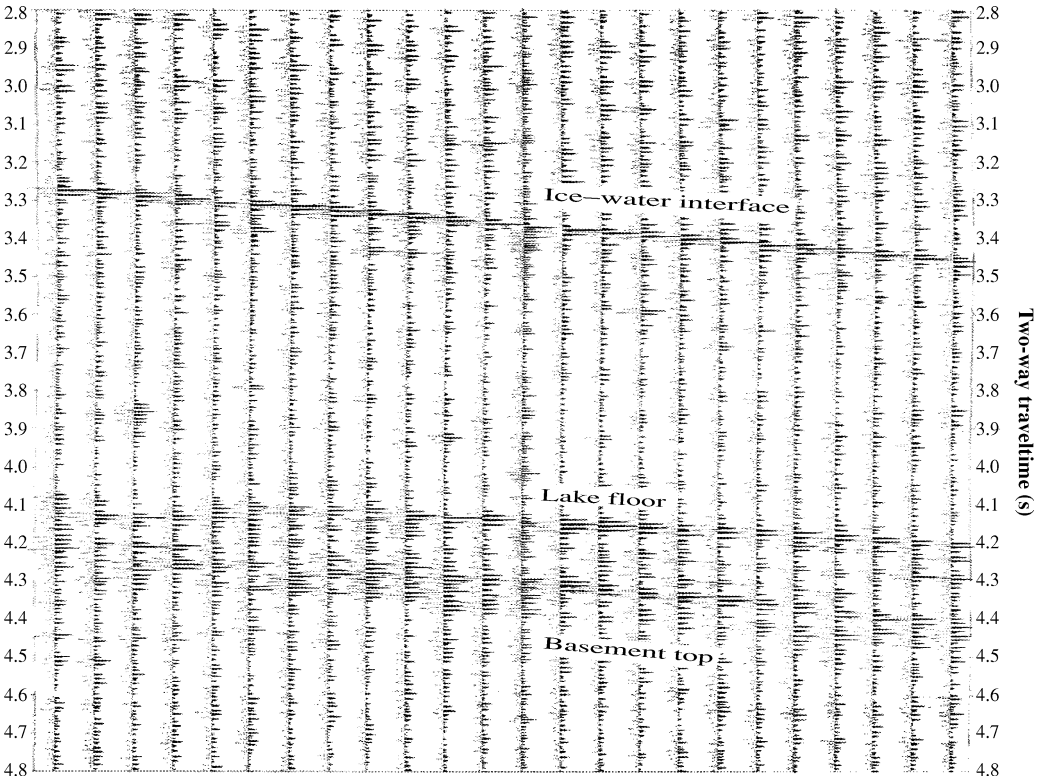

Figure 2 Example of a 24-channel seismic record from line 2-2′. The distance from the shotpoint to the nearest trace is 4 km (Masolov *et al.* 1999). We have noticed a discrepancy between the two-way traveltime of this record and the traveltime obtained from the VSP survey (see fig. 7 of Masolov *et al.* 1999).

SH-waves, because our modelling is based on P- and SV-waves. Pure-ice density is $\rho_i = 919$ kg/m^3 (Angenheister 1982).

The first layer is unconsolidated ice (firn: snow recrystallized into granules) with relatively low wave velocities and density. We consider a constant-velocity layer, but a parabolic velocity profile (Thiel and Ostenso 1961; King and Jarvis 1991) may also be assumed. The P-wave velocity given in Table 1 is from Masolov *et al.* (1999). We use the model given in Appendix A.3 and the data of Table 3 (Johnson 1982) to obtain the seismic properties of firn. Firn is assumed to be isotropic, viscoelastic and porous, with pure ice constituting the solid phase. We assume firn to have random crystal orientations and to be unconsolidated. Pure ice is assumed to have a bulk modulus $K_i = c_{33} - 4c_{55}/3$ to obtain the seismic properties of firn. Wave dissipation is introduced as indicated in Appendix A.3 (equations (A17) and (A18)).

The underlying ice sheet (blue ice 1: low-pressure polymorph ice Ih) is transversely isotropic, with the elastic constants given in (1) at $z = 100$ m depth. The elastic constants at 2600 m depth are obtained by assuming $V_P = 3920$ m/s, and the same anisotropy parameters of the layer top (see Table 1 and Appendix A.4), and $V_P/V_S = 2.14$ corresponding to (1). We obtain

$$\begin{aligned} c_{11} &= 15.82\,\text{GPa}, \quad c_{13} = 6.44\,\text{GPa}, \\ c_{33} &= 14.44\,\text{GPa}, \quad c_{55} = 3.15\,\text{GPa}, \end{aligned} \tag{2}$$

which give a vertical P-wave velocity in agreement with Masolov *et al.* (1999) (the constants in (1) and (2) differ by a factor of nearly 1.04). The density at 2600 m is assumed to be $\rho_i = 925$ kg/m^3 due to compaction effects. The seismic properties of this layer – including the density – are linearly interpolated from 100 m to 2600 m. The associated quality factors (see Table 1) are assumed to model attenuation due to the presence of sediments and ice flow.

The layers between 2600 and 3500 m have the vertical P-wave velocity obtained by Masolov *et al.* (1999) from VSP experiments and $V_S = V_P/2.14$. The anisotropy parameters are the same as those for the blue-ice 1 layer (see Table 1). The seismic velocity in 'blue ice 4' is abnormally high. Masolov *et al.* (1999) acknowledge that this value is abnormally high but do not discuss a justification of errors. It is significantly higher than would be expected for the maximum P-wave

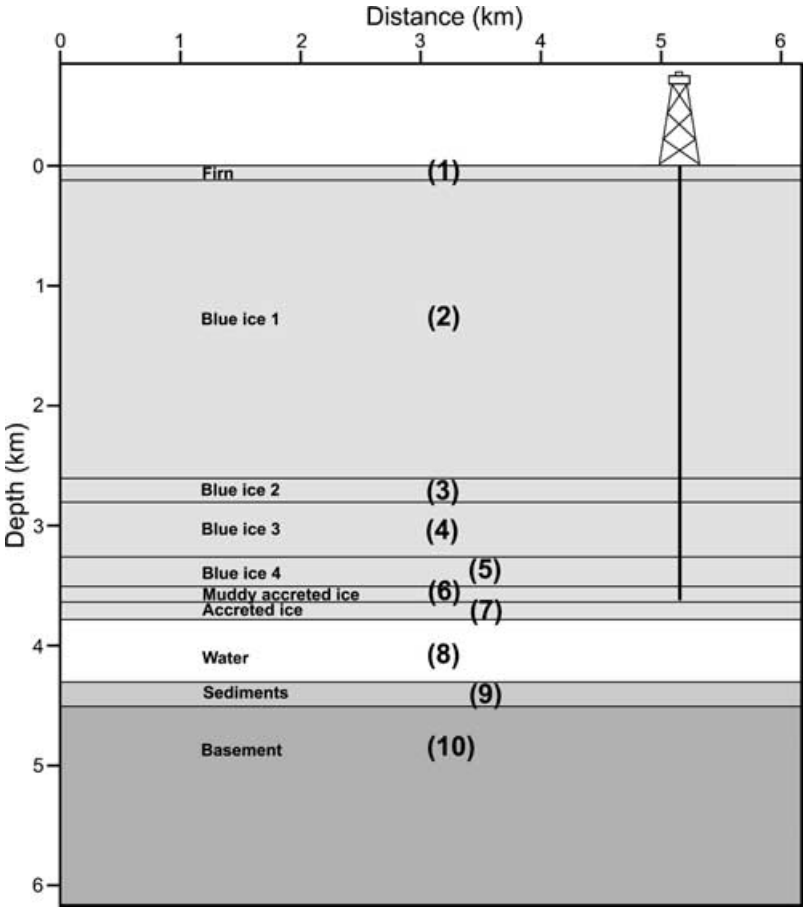

Figure 3 Seismic model of Lake Vostok. The material properties are given in Table 1.

Table 1 Lake Vostok model: seismic properties. High-frequency limit or unrelaxed wave velocities ($V_P = \sqrt{c_{33}/\rho}$, $V_S = \sqrt{c_{55}/\rho}$), density, anisotropy parameters and quality factors, which parametrize the attenuation of the dilatational and shear deformations*

Layer	Medium	Depth† (m)	V_P (m/s)	V_S (m/s)	ρ (kg/m^3)	ϵ	δ	Q_1	Q_2
1	Firn	100	1645	1089	506	0	0	30	20
2	Blue ice 1 (top)		3886	1816	919	0.05	−0.1	100	80
2	Blue ice 1 (bottom)	2600	3920	1832	925	0.05	−0.1	100	80
3	Blue ice 2	2800	3820	1786	925	0.05	−0.1	100	80
4	Blue ice 3	3250	3910	1828	925	0.05	−0.1	100	80
5	Blue ice 4	3500	4120	1926	925	0.05	−0.1	100	80
6	Accreted ice (mud)	3600	3720	1735	922	0	0	60	40
7	Accreted ice (gas)	3750	3709	1745	912	0	0	80	60
8	Water	4290	1443	0	1017	0	0	∞	–
9	Sediment	4490	2817	1530	2128	0	0	20	15
10	Bedrock		5200	3040	3200	0.1	0	200	180

*Q_1 and Q_2 are attenuation parameters. The P-wave and S-wave quality factors are functions of these parameters, the elasticity coefficients and the propagation direction (Carcione, Cavallini and Helbig 1998).
†Base of layer.

Table 2 Seismic properties of ice (Angenheister 1982)

c_{IJ}	A_0 (GPa)	A_1 (GPa °C^{-1})	A_2 (GPa °C^{-2})
c_{11}	14.075	-2.293×10^{-2}	-4.124×10^{-5}
c_{13}	5.622	-1.053×10^{-2}	0
c_{33}	12.904	-1.921×10^{-2}	-2.387×10^{-5}
c_{55}	2.819	-0.451×10^{-2}	-1.02×10^{-5}

Table 3 Seismic properties of firn

Grain	$\rho_s = 919$ kg/m^3
	$K_s = 9.8$ GPa
Air	$\rho_a = 1.61$ kg/m^3
	$K_a = 0.135$ MPa
Matrix	$\rho = 506$ kg/m^3
	$K_m = 0.57$ GPa*
	$\mu_m = 0.6$ GPa*
	$\phi = 0.45$*
	$\mathcal{T} = 2$

*Johnson (1982).

velocity parallel to the *c*-axis of a pure ice crystal (around 4020–4030 m/s) (Angenheister 1982). Blue ice 2–4 have the structure of ice Ih, with the differences in velocity being due to compaction. We assume no major density variations for these layers and consider the same value as blue ice 1.

The ice at the base of the ice-sheet layer is subjected to melting and freezing processes (Layers 6 and 7, Table 1, Fig. 3). Changes in ice character are significant, with an increase in crystal size (to 10–100 cm) (and a consequent increase in porosity) and a decrease in the electric conductivity, possibly due to the presence of highly dielectric media such as mud and air. Therefore, we assume that these physical and chemical changes represent refrozen or accreted ice, filled with mud between 3500 and 3600 m depth and with air between 3600 m depth and the ice/water interface (Bell 1998). We assume that the melting and refreezing process results in the development of random crystal orientations, which makes these layers mechanically isotropic. We further assume that they have the velocities obtained by Masolov *et al.* (1999) from VSP measurements. Using the composite model introduced in Appendix A.5 and the velocity obtained by Masolov *et al.* (1999), we calculate the saturation of mud in the first accreted layer to be 1.3% (layer 6), assuming a sound velocity of 1500 m/s and a density of 1200 kg/m^3 for mud.

Table 4 Seismic properties of the sediment

Grain	$\rho_s = 2650$ kg/m^3
	$K_s = 39$ GPa
Water	$\rho_w = 1019$ kg/m^3
	$K_w = 2.16$ GPa
Matrix	$K_m = 6.2$ GPa
	$\mu_m = 4.6$ GPa
	$\phi = 0.32$
	$\mathcal{T} = 2$

The seismic properties of the second layer (layer 7, filled with air) are calculated by considering a similar porosity (Masolov *et al.* (1999) do not provide the velocity for this layer). We assume the medium to be isotropic, i.e. that the crystallization is randomly orientated in those layers. The conditions at 3500 m are $T = -6.7$°C and $p = 31.6$ MPa, assuming a basal temperature $T(z = 3750\text{ m}) = -3.26$°C and a linear interpolation between the ice/water interface and the surface. Pure-ice density is taken as $\rho_i = 919$ kg/m^3, the elastic constants are calculated using (A19), and the bulk modulus is obtained as $K_i = c_{33} - 4c_{55}/3 = 9.8$ GPa. The seismic properties of *in situ* air are obtained from (A5) ($\rho_a = 371$ kg/m^3) and (A8) ($K_a = 81$ MPa), assuming the temperature and pressure profiles given in (A1) and (A4), respectively ($T = -5.32$°C and $p = 32.5$ MPa at 3600 m depth).

The lake is assumed to be composed of fresh water. The seismic properties of fresh water at the *in situ p–T* conditions ($T = -3.26$°C and $p = 33.8$ MPa) are computed using the empirical equations provided by Batzle and Wang (1992) (see Mavko, Mukerji and Dvorkin 1998). Water is assumed to be lossless. Finally, Biot's theory is used to obtained the unrelaxed wave velocities of the sediment layer, given the properties of the solid grains (a mixture of quartz and clay), the solid skeleton and water at *in situ* conditions ($T = -3.26$°C and $p = 39.2$ MPa) (see Table 4). The matrix dry-rock moduli have been assumed to be those of a typical sediment at 4.5 km depth. Note that the different properties of pore water compared with lake water are due to the different pressure conditions.

THEORETICAL AVA CURVES

Amplitude variations with angle (AVA) methods can be used to identify the interfaces associated with subglacial lakes. The reflection coefficients of the ice/water and water/sediment interfaces are obtained in Appendices B.1 and B.2, respectively. Figure 4 shows the PP and PS reflection coefficients and PP transmission coefficient, for the accreted ice/water interface.

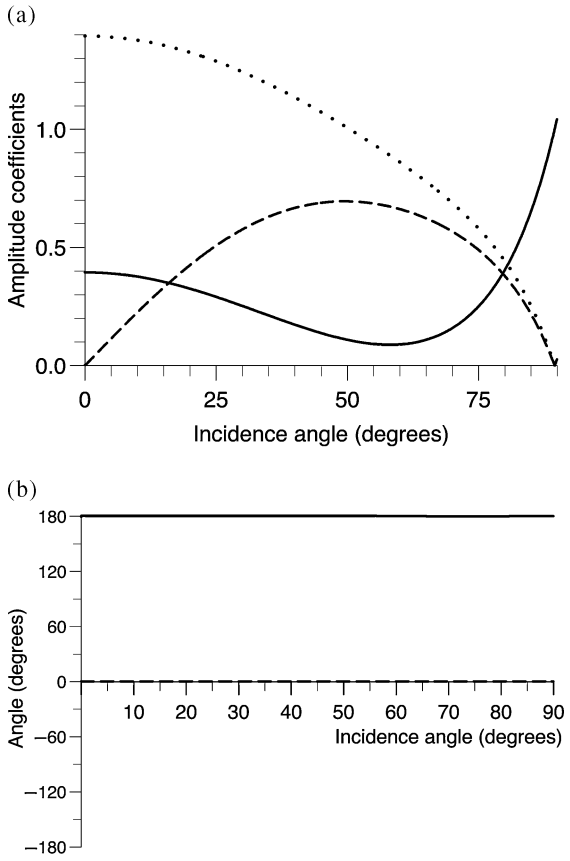

Figure 4 (a) PP and PS reflection coefficients (solid and dashed lines, respectively) and PP transmission coefficient (dotted line) and (b) phase angles, for the ice/water interface.

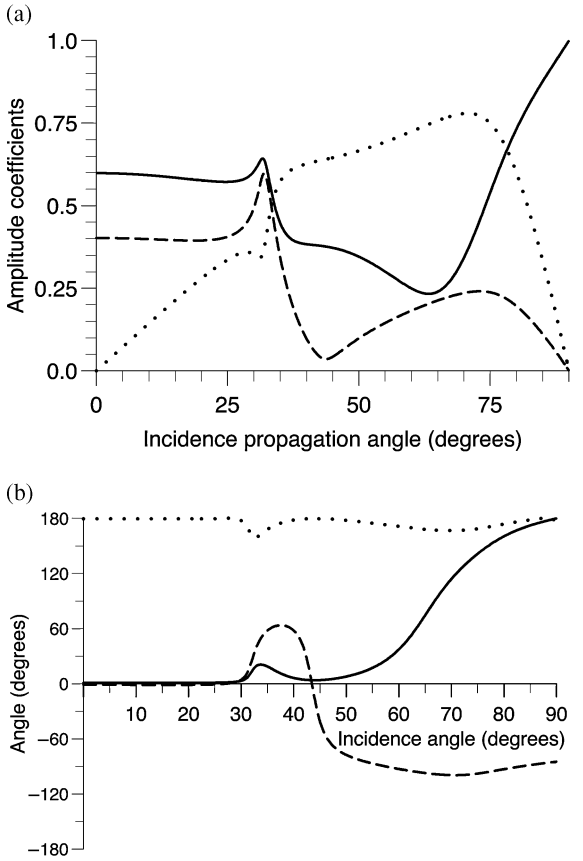

Figure 5 PP (solid line) reflection coefficient and phase, and PP (dashed line) and PS (dotted line) transmission coefficients and phases, for the water/sediment interface.

The PP amplitude anomaly is negative at near offsets (the amplitude decreases with increasing angle), with a minimum at nearly 56°. There are no critical angles since the P-wave and S-wave velocities of the ice are greater than the sound velocity of water. The PS anomaly is positive at near offsets.

The reflection coefficients corresponding to the water/sediment interface are shown in Fig. 5, where the solid, dashed and dotted lines indicate the PP reflection coefficient (absolute value) and the PP and PS transmission coefficients (absolute values) and phases, respectively. Although critical angles are rare for interfaces separating viscoelastic media (Carcione 1997), this effect can be seen at an angle of incidence of nearly 31° ($\approx \sin^{-1}$ (1443/2817), according to Snell's law). However, the effects of the other critical angle, due to the S-wave, which in the lossless case appears at an angle of incidence of 71° ($\sin^{-1}$ (1443/1530)), is not evident in Fig. 5. The PP reflection anomaly of the water/sediment interface is almost constant at near offsets (0–25°). The top of the lake can be identified by the negative anomaly in the PP reflection coefficient, since the same coefficient corresponding to the bottom of the lake is almost flat at the near offsets. Moreover, the bottom of the lake does not have a PS reflection event.

In summary, our models show that the near-offset AVA of subglacial-lake tops (ice-over-water contacts) is characterized by a PP negative anomaly and a PS positive anomaly. In contrast, the near-offset AVA of subglacial-lake bottoms (water-over-sediment contacts) is a flat response.

SIMULATIONS

The time-domain equations for wave propagation in a heterogeneous, viscoelastic and transversely isotropic medium can be found in Carcione (1995). The differential equations are given in Appendix C. The anelasticity is described by the standard linear solid, also known as the Zener model (Zener 1948).

The notation used in Carcione (1995) denotes the relaxed or low-frequency limit stiffnesses by c_{IJ}, and the unrelaxed or high-frequency limit elastic constants by $\hat{c}_{IJ}$. In order to use the standard notation and define the purely elastic limit in the unrelaxed regime, we denote the unrelaxed stiffnesses by c_{IJ}, as indicated in Table 1.

The modelling algorithm is based on a 4th-order Runge–Kutta time-integration scheme and the staggered Fourier method to compute the spatial derivatives (e.g. Carcione and Helle 1999). The mesh has 616 × 616 points, with a grid spacing of 10 m (this grid size is sufficient to sample the shortest wavelengths, according to the Nyquist theorem). In order to avoid wraparound, absorbing strips of 50 gridpoints length are implemented at the boundaries of the numerical mesh. The source is a dilatation force ($f_x = f_z = 0, f_{xx} = f_{zz} \neq 0, f_{xz} = 0$, see Appendix C), whose time-history is a Ricker wavelet. It is located at 120 m depth (gridpoints (70,12)), and has a dominant frequency of $f_d = 25$ Hz. The wavefield is computed by using a time step of 1 ms with a maximum time of 3.5 s. The vertical particle-velocity component recorded at the surface is shown in Fig. 6, where the straight events are a wave travelling with the P-wave velocity of the ice layer (P), and a train of waves travelling in the firn layer (D) (Rayleigh waves are not modelled by the present algorithm). The two main reflection events (PP2 and PP3) correspond to the ice/water and water/sediment interfaces (at approximately 2 s and 2.7 s zero-offset traveltimes). These reflections have opposite polarity (compare Figs 4b and 5b). The reflection due to the sediment/basement interface has a zero-offset traveltime of nearly 2.8 s (PP4). The events PP2, PP3 and PP4 are the three reflections observed in the real seismogram (see Fig. 2). Weaker reflections within the ice sheet can be seen before reflection PP2. Modelling layers 2–5 and 6–7 as average single layers yields amplitude differences that affect the AVA curves of the lower interfaces. Firstly, less seismic energy reaches the top of the lake, because of reflection and anelasticity. Secondly, although the reflections from these layers cannot be observed in the real seismograms, the layers act as a filter. The effect is to reduce the large-offset AVA response of the lower layers. The same argument applies to the use of an isotropic stress–strain relationship for the ice sheet. A snapshot of the wavefield at 2 s propagation time is shown in Fig. 7. This figure gives a clear picture of the nature, location and relative amplitudes of the different events associated with the lake. A ray-tracing modelling is illustrated in Fig. 8. The velocity inversion at the lake

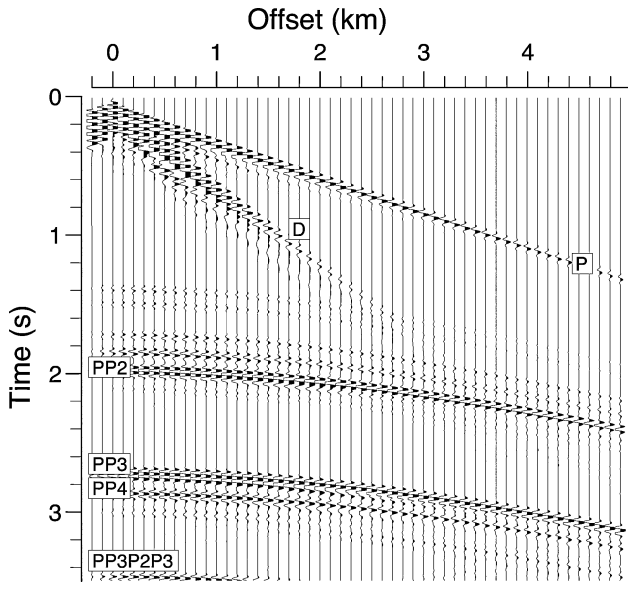

Figure 6 Synthetic seismogram of the vertical particle-velocity component recorded at the surface. The events are the wave travelling in the ice layer (P), a train of waves travelling with the P-wave velocity of firn (D), the reflections from the ice/water (PP2), water/sediment (PP3) and sediment/basement (PP4) interfaces, and a reverberation inside the lake (PP3P2P3).

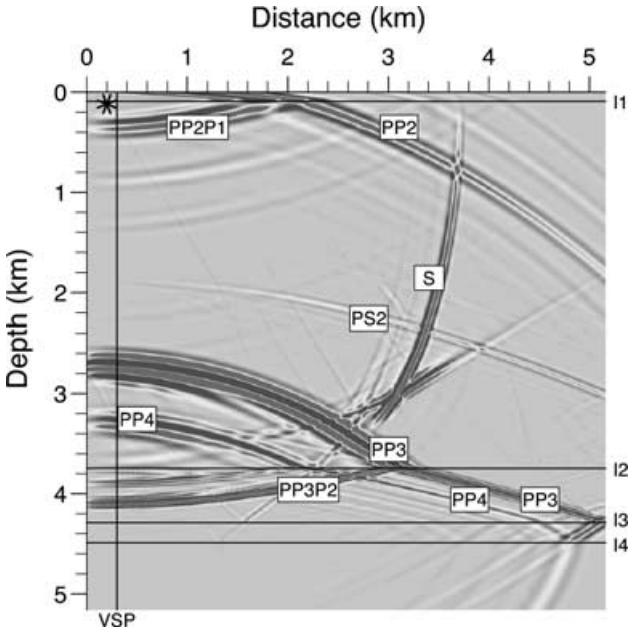

Figure 7 Snapshot of the vertical particle-velocity component at 2 s propagation time, where S is the direct shear wave, PP2, PP3 and PP4 are the PP reflections at the ice/water, water/sediment and sediment/basement interfaces (I2, I3 and I4, respectively), PS2 is the PS conversion at the ice/water interface (I2), and the down-going events PP2P1 and PP3P2 are the reflections of PP2 and PP3 at the firn/ice (I1) and ice/water (I2) interfaces, respectively.

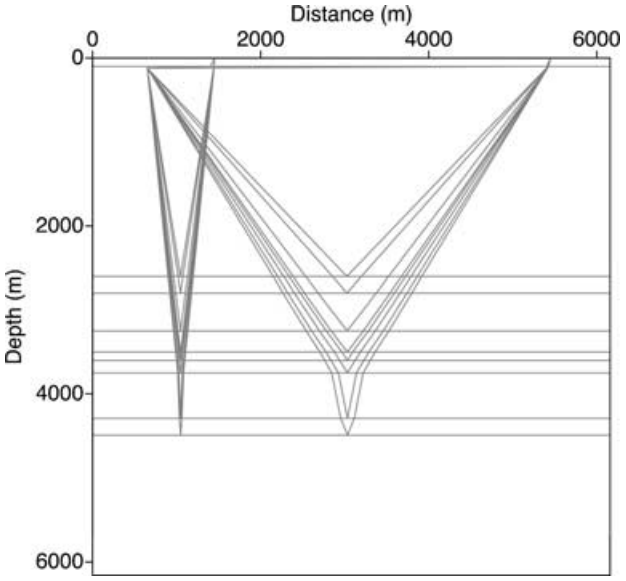

Figure 8 Ray-tracing of the main reflections associated with the Lake Vostok model.

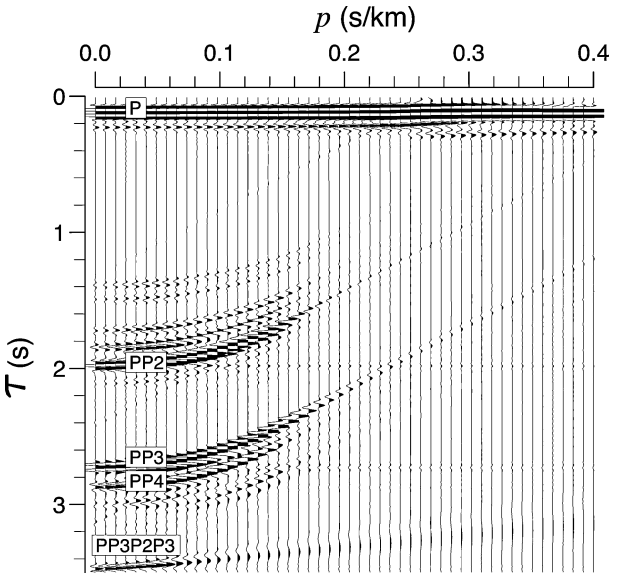

Figure 10 Slant stack of the seismogram shown in Fig. 6. The labels represent the different events described in the caption of Fig. 7.

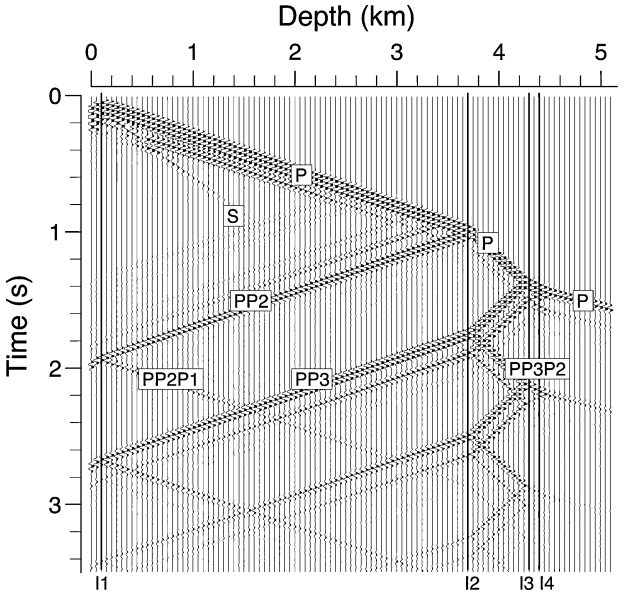

Figure 9 Synthetic vertical seismic profile at 100 m from the source location. The labels represent the different events described in the figure caption of Fig. 7 (P is the transmitted P-wave from the source to the basement), while I1, I2, I3 and I4 indicate the firn/ice, ice/water, water/sediment and sediment/basement interfaces.

reduces the offset of the water/sediment reflection. Figure 9 shows a synthetic VSP, corresponding to the vertical particle-velocity component, where the source–well distance is 100 m. Changes in the slopes of the events indicate the location of the interfaces in one-way traveltime. Unfortunately, there is no published picture of a real VSP recorded at the Vostok station to perform a visual comparison with the synthetic VSP shown in Fig. 9.

A τ–p transform, slant stack or plane-wave decomposition, applied to a reflection seismogram can be used for many purposes, such as velocity analysis, multiple elimination, filtering of direct and surface waves, etc. (Treitel, Gutowski and Wagner 1982; Gardner and Lu 1990; Wang and Houseman 1997). Plane-wave decomposition of a common-shot gather (such as the seismogram shown in Fig. 6) is performed by applying a linear moveout (LMO) correction and summing amplitudes over the offset axis. The slant stack of the reflection seismogram shown in Fig. 6 is displayed in Fig. 10. The direct events are clearly visible at the beginning of the slant stack, and the three reflections, corresponding to the ice/water (PP2), water/sediment (PP3) and sediment/basement (PP4) interfaces, map on to three quasi-elliptical events.

We can use seismic amplitude variations with offset (or angle) (AVO or AVA) to identify the top of the lake on the basis of different AVA anomalies. Consider the PP2 event in Fig. 6, corresponding to the ice/water interface. We picked the average amplitude of the vertical particle-velocity component, after correction for radiation pattern, geometrical spreading and intrinsic loss. Because the modelling is two-dimensional, the geometrical spreading correction is $\sqrt{R}$, where R is the travel-path. If the data are normalized with respect to the zero-offset trace, the correction factor becomes $1/\sqrt{\cos\theta}$, where θ is the

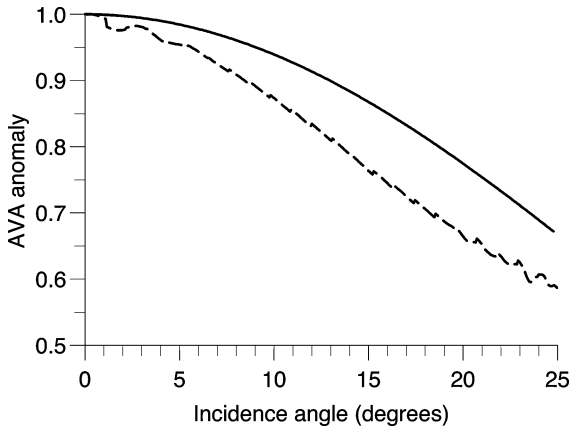

Figure 11 Comparison between the AVA curve of the ice/water interface (PP2 in Fig. 6) (dashed line) and the theoretical vertical particle-velocity component (solid line).

incidence propagation angle measured from the vertical axis. The loss correction factor is approximately $\exp[\alpha(R - 2h)]$, where α is the attenuation factor and h is the vertical distance from the source to the interface. Since $\alpha \approx \pi f_{\mathrm{d}}/(V_{\mathrm{P}}Q_{\mathrm{P}})$ (Toksöz and Johnston 1981), where V_{P} and Q_{P} are averages of the P-wave velocity and quality factor, the correction is $\exp[2\pi h f_{\mathrm{d}}(-1 + 1/\cos\theta)/(V_{\mathrm{P}}Q_{\mathrm{P}})]$. We consider $V_{\mathrm{P}} = 3900$ m/s and $Q_{\mathrm{P}} = 90$. The P-wave quality factor satisfies the inequality $Q_2 < Q_{\mathrm{P}} < Q_1$ when $Q_2 < Q_1$, where Q_1 and Q_2 are the dilatational and shear quality factors. Figure 11 compares the picks (dashed line) with the theoretical particle-velocity component $v_z = \mathrm{real}(\mathrm{i}\omega\gamma_{\mathrm{P}_1}R_{\mathrm{PP}})$ (solid line) for the ice/water interface (see Appendix B.1). The differences between the solid and dashed lines can be attributed to transmission effects due to the presence of layering in the ice sheet (PP reflection and PS conversion). Picking of synthetic amplitudes in the τ–p domain has confirmed the trend observed in Fig. 11. An AVA analysis of the base of the lake (not shown here) confirms the trend observed in Fig. 5(a). On the basis of these AVA analyses, the PP anomaly of the top of the lake is negative (amplitude decreases with angle of incidence), while the PP AVA trend of the base of the lake is almost constant. This difference allows the identification of the lake interfaces.

CONCLUSIONS

Rock-physics models, seismic theory and numerical modelling of wave propagation have been used to analyse the seismic response of a subglacial lake. We have achieved a complete seismic characterization of the different layers, the shallow firn layer, the thick ice sheet and the lake, including the sediments and the bedrock. The stronger reflections are those associated with the ice/water (PP2), water/sediment (PP3) and sediment/basement (PP4) interfaces. The reflection coefficients of the top and bottom of the lake show distinct characteristics, which allow their identification from seismic records by using AVA methods. Reflections PP2 and PP3 have opposite polarity. Reflections PP3 and PP4 can hardly be resolved for sediment thicknesses less than 200 m. Other weaker events are the reflections inside the ice sheet and reverberations inside the lake. The methodology introduced in this paper, based on rock physics and numerical modelling, can be used to characterize the seismic response of any subglacial lake, and aid the planning of seismic surveys.

ACKNOWLEDGMENTS

We acknowledge Hans B. Helle from Norsk Hydro (Bergen) for providing useful data about the seismic properties of ice and the *in situ* conditions in polar regions. We thank the Associate Editor Y. Wang and an anonymous reviewer for a very detailed and useful review.

REFERENCES

Angenheister G. (ed.) 1982. *Physical Properties of Rocks*, Vol. 1b, Landolt-Börnstein (ed. K.H. Hellwege). Springer-Verlag, Inc.

Batzle M. and Wang Z. 1992. Seismic properties of pore fluids. *Geophysics* **57**, 1396–1408.

Bell R.E. 1998. Lake Vostok: Background information. Review of Lake Vostok studies, Lake Vostok Workshop, Washington, DC.

Ben-Menahem A. and Singh S.G. 1981. *Seismic Waves and Sources*. Springer-Verlag, Inc.

Carcione J.M. 1995. Constitutive model and wave equations for linear, viscoelastic, anisotropic media. *Geophysics* **60**, 537–548.

Carcione J.M. 1997. Reflection and transmission of *qP*–*qS* plane waves at a plane boundary between viscoelastic transversely isotropic media. *Geophysical Journal International* **129**, 669–680.

Carcione J.M. 1998. Viscoelastic effective rheologies for modelling wave propagation in porous media. *Geophysical Prospecting* **46**, 249–270.

Carcione J.M., Cavallini F. and Helbig K. 1998. Anisotropic attenuation and material symmetry. *Acustica* **84**, 495–502.

Carcione J.M. and Helle H.B. 1999. Numerical solution of the poroviscoelastic wave equation on a staggered mesh. *Journal of Computational Physics* **154**, 520–527.

Carcione J.M. and Helle H.B. 2002. Rock physics of geopressure and prediction of abnormal pore fluid pressures using seismic data. *CSEG Recorder* **27**(7), 8–32.

Friedman A.S. 1963. Pressure–volume–temperature relationships of gases, virial coefficients. In: *American Institute of Physics Handbook*. McGraw-Hill Book Co.

Gardner G.H.F. and Lu L. 1990. Slant-stack processing. In: *Some Fundamentals of Slant-Stack Methods* (Appendix 1). Geophysical Reprint Series No. 14. Society of Exploration Geophysicists.

Gurevich B. 1996. Discussion on: "Wave propagation in heterogeneous, porous media: A velocity-stress, finite difference method" by N. Dai, A. Vafidis, and E.R. Kanasewich (March–April 1995, *Geophysics* pp. 327–340). *Geophysics* **61**, 1230–1232.

Johnson J.B. 1982. On the application of Biot's theory to acoustic wave propagation in snow. *Cold Regions Science and Technology* **6**, 49–60.

Jouzel J., Barkov N.I., Barnola J.M., Bender M., Chappellaz J., Genthon C. *et al.* 1993. Extending the Vostok ice-core record of paleoclimate to the penultimate glacial period. *Nature* **364**, 407–412.

Kapitsa A.P., Ridley J.K., Robin G. de Q., Siegert M.J. and Zotikov I.A. 1996. A large deep freshwater lake beneath the ice of central East Antarctica. *Nature* **381**, 684–686.

King E.C. and Jarvis E.P. 1991. Effectiveness of different shooting techniques in Antarctic firn. *First Break* **9**, 281–288.

Kuster G.T. and Toksöz M.N. 1974. Velocity and attenuation of seismic waves in two-phase media: Part I. Theoretical formulations. *Geophysics* **39**, 587–606.

Mahan B.H. and Myers R.J. 1987. *University Chemistry*. The Benjamin/Commings Pub. Co.

Masolov V.N., Kudryavtzev G.A., Sheremetiev A.N., Popkov A.M., Popov S.V., Lukin V.V., Grikurov G.E. and Leitchenkov G.L. 1999. Earth science studies in the Lake Vostok region: existing data and proposals for future research. SCAR International Workshop on Subglacial Lake Exploration, Cambridge, England.

Mavko G., Mukerji T. and Dvorkin J. 1998. *The Rock Physics Handbook: Tools for Seismic Analysis in Porous Media*. Cambridge University Press, Cambridge, UK.

Morse P.M. and Ingard K.U. 1986. *Theoretical Acoustics*. Princeton University Press, Princeton, NJ.

Paterson W.S.B. 1994. *The Physics of Glaciers*, 3rd edn. Pergamon Press Inc.

Petit J.R. 1998. Evidence from the Vostok ice core studies. Review of Lake Vostok studies, Lake Vostok Workshop, Washington, DC.

Petit J.R., Basile I., Leruyuet A., Raynaud D., Lorius C., Jouzel J. *et al.* 1997. Four climate cycles in Vostok ice core. *Nature* **387**, 359.

Ridley J.K., Cudlip W. and Laxon S.W. 1993. Identification of subglacial lakes using ERS-1 radar altimeter. *Journal of Glaciology* **39**, 625–634.

Robin G. de Q. 1955. Ice movement and temperature distribution in glaciers and ice sheets. *Journal of Glaciology* **3**, 589–606.

Robin G. de Q., Drewry D.J. and Meldrum D.T. 1977. International studies of ice sheet and bedrock. *Philosophical Transactions of the Royal Society of London* **279**, 185–196.

Siegert M.J. 2000. Antarctic subglacial lakes. *Earth-Science Reviews* **50**, 29–50.

Siegert M.J. and Dowdeswell J.A. 1996. Spatial variations in heat at the base of the Antarctic ice sheet analysis of the thermal regime above subglacial lakes. *Journal of Glaciology* **42**, 501–509.

Siegert M.J. and Ridley J.K. 1998. An analysis of the ice-sheet surface and subsurface topography above the Vostok Station subglacial lake, central East Antarctica. *Journal of Geophysical Research* **103**(B5), 10195–10207.

Standing M.B. 1952. *Volumetric and Phase Behaviour of Oil Field Hydrocarbon Systems*. Reinhold Publishing Corp., New York.

Thiel E. and Ostenso N.A. 1961. Seismic studies on antarctic ice shelves. *Geophysics* **26**, 706–715.

Thomsen L. 1986. Weak elastic anisotropy. *Geophysics* **51**, 1954–1966.

Toksöz M.N. and Johnston D.H. 1981. *Seismic Wave Attenuation, Definitions and Terminology* (Chapter 1). Geophysical Reprint Series No. 2. Society of Exploration Geophysicists.

Treitel S., Gutowski P.R. and Wagner D.E. 1982. Plane-wave decomposition of seismograms. *Geophysics* **47**, 1375–1401.

Wang Y. and Houseman G.A. 1997. Point-source τ–p transform: a review and comparison of computational methods. *Geophysics* **62**, 325–334.

Wüest A. and Carmack E. 2000. A priori estimates of mixing and circulation in the hard-to-reach water body of Lake Vostok. *Ocean Modelling* **2**, 29–43.

Yew C.H. and Weng X. 1987. A study of reflection and refraction of waves at the interface of water and porous sea ice. *Journal of the Acoustical Society of America* **82**(1), 342–353.

Zener C. 1948. *Elasticity and Anelasticity of Metals*. University of Chicago Press.

APPENDIX A

Rock-physics models

A.1 Temperature and pressure profiles of the ice sheet

Pressure and temperature information is necessary to obtain the seismic properties of firn, ice, refrozen or accreted ice and water. The presence of subglacial lakes implies that the temperature of the ice-sheet base is at the pressure melting point (Siegert and Dowdeswell 1996). A model for the temperature profile of the ice sheet has been given by Robin (1955). Assuming a linear geothermal gradient through the ice sheet, the temperature profile at depth z is

$$T = T_S + \frac{\sqrt{\pi}\eta\Lambda}{2Ch}\mathrm{erf}\left(\frac{h}{\eta}\right)z, \tag{A1}$$

where

$$\eta = \left(\frac{2kh}{B}\right)^{1/2}, \tag{A2}$$

$\mathrm{erf}(\cdot)$ is the error function, T_S is the mean annual surface temperature ($T_S = -55^\circ$C at the Vostok station; Petit *et al.* 1997), Λ is the earth's geothermal heat flux (54 mW/m^2) (e.g. Wüest and Carmack 2000), C is the thermal conductivity of ice (2.1 W m^{-1} $^\circ$C^{-1}), h is the thickness of the ice sheet above the lake (m), k is the thermal diffusivity of ice (36.3 m^2/year) and

B is the mean annual surface accumulation of the ice sheet above the lake (2 cm/year; Jouzel *et al.* 1993).

The pressure melting point temperature of pure ice, in °C, is

$$T_{\mathrm{pmp}} = -\frac{h}{1149} \tag{A3}$$

(Siegert and Dowdeswell 1996), which corresponds to a Clausius–Clayperon gradient of 8.7×10^4 °C/m (Paterson 1994). Equation (A1) holds only if the basal temperature $T(h)$ is at or below the pressure melting point. If $T(h) > T_{\mathrm{pmp}}$, the basal temperature should be taken equal to T_{pmp}.

The pressure profile is estimated by standard techniques (e.g. Carcione and Helle 2002), although it is expected that variations due to the particular *in situ* conditions may occur. The pressure profile versus depth is

$$p = \rho_{\mathrm{i}} g z, \tag{A4}$$

where $\rho_{\mathrm{i}} = 919$ kg/m^3 is the density of ice and $g = 9.81$ m/s^2. The estimated pressure at the base of the ice sheet ($z = 3750$ m) is then approximately 34 MPa.

A.2 *Acoustic properties of polar air*

Air behaves as a real gas, which satisfies approximately the van der Waals equation (Friedman 1963):

$$\left(p + a\rho_{\mathrm{a}}^2\right)(1 - b\rho_{\mathrm{a}}) = \rho_{\mathrm{a}} R(T + 273), \tag{A5}$$

where p is the pressure (in Pa), ρ_{a} is the density (in kg/m^3) and $R = 8.31448$ J/(mol °K) is the gas constant ($R = 288.5$ J/(kg °K) for air (20% O_2 plus 80% N_2), since 1 mol = 28.8 g). Moreover, for air, $a = 1.65 \times 10^{-4}$ MPa m^6 kg^{-2} and $b = 1.29 \times 10^{-3}$ m^3 kg^{-1} (Mahan and Myers 1987). Equation (A5) gives the air density as a function of pressure and temperature.

The isothermal compressibility c_{T} depends on pressure. It can be calculated from van der Waals equation (A5) using

$$c_{\mathrm{T}} = \frac{1}{\rho_{\mathrm{a}}}\frac{\partial \rho_{\mathrm{a}}}{\partial p}, \tag{A6}$$

which gives

$$c_{\mathrm{T}} = \left[\frac{\rho_{\mathrm{a}} RT}{(1 - b\rho_{\mathrm{a}})^2} - 2a\rho_{\mathrm{a}}^2\right]^{-1}. \tag{A7}$$

For sound waves below 1 GHz, it is a better approximation to assume that the compression is adiabatic, i.e. that the entropy content of the air remains nearly constant during the compression (Morse and Ingard 1986). Adiabatic compressibility c_{S} is related to isothermal compressibility c_{T} by $c_{\mathrm{S}} = c_{\mathrm{T}}/\gamma$, where γ is the heat capacity ratio at constant pressure, which depends on measurable quantities (Morse and Ingard 1986). For polyatomic gases we may use the approximation $\gamma \approx 4/3$ (Morse and Ingard 1986). In this case, the air bulk modulus can expressed as

$$K_{\mathrm{a}} = \frac{1}{c_{\mathrm{S}}} = \frac{\gamma}{c_{\mathrm{T}}} = \frac{4}{3c_{\mathrm{T}}}. \tag{A8}$$

It can be shown that (A5) can be a good approximation to the behaviour of multicomponent gases, since the differences between the experimental data, as represented by Standing's results (Standing 1952), and the van der Waals results are only about 15% over the depths of interests. An alternative but similar expression for the acoustic properties of gases can be found in Batzle and Wang (1992) and Mavko *et al.* (1998).

A.3 *Seismic model for firn and sediment*

Biot's theory of dynamic poroelasticity is used to compute the unrelaxed wave velocities of firn. This theory was shown to be appropriate for describing wave propagation in snow (Johnson 1982). Neglecting the viscosity of air, the velocities of the fast (+ sign) and slow (− sign) compressional waves and shear wave are given by (see e.g. Carcione 1998)

$$V_{\mathrm{P}\pm}^2 = \frac{A \pm \sqrt{A^2 - 4ME\bar{\rho}\rho_1}}{2\bar{\rho}\rho_1} \tag{A9}$$

and

$$V_{\mathrm{S}}^2 = \frac{\mu_m}{\bar{\rho}}, \tag{A10}$$

where

$$A = M(\rho - 2\alpha\rho_{\mathrm{f}}) + \rho_1(E + \alpha^2 M), \tag{A11}$$

$$\bar{\rho} = \rho - \frac{\phi\rho_{\mathrm{f}}}{\mathcal{T}}, \quad \rho_1 = \frac{\mathcal{T}}{\phi}\rho_{\mathrm{f}}, \tag{A12}$$

with α and E denoting the elastic coefficients and $\mathcal{T}$ denoting the tortuosity. The sediment density is given by

$$\rho = (1 - \phi)\rho_{\mathrm{s}} + \phi\rho_{\mathrm{f}},$$

where ρ_{s} and ρ_{f} are the solid and fluid densities, respectively.

The elastic coefficients are given by

$$E = K_{\mathrm{m}} + \frac{4}{3}\mu_{\mathrm{m}}, \tag{A13}$$

$$M = \frac{K_{\mathrm{s}}^2}{D - K_{\mathrm{m}}}, \tag{A14}$$

$$D = K_{\mathrm{s}}\left[1 + \phi\left(K_{\mathrm{s}}K_{\mathrm{f}}^{-1} - 1\right)\right], \tag{A15}$$

$$\alpha = 1 - \frac{K_{\rm m}}{K_{\rm s}}, \tag{A16}$$

where $K_{\rm m}$ and $\mu_{\rm m}$ are the dry-rock moduli, $K_{\rm f}$ is the bulk modulus of the fluid and $K_{\rm s}$ is the bulk modulus of the grains. The stiffness E is the P-wave modulus of the dry skeleton, M is the elastic coupling modulus between the solid and the fluid, and α is the poroelastic coefficient of effective stress. The same model is used to calculate the sediment properties, given the dry-rock bulk moduli.

The following attenuation model assumes a single standard linear solid element (Ben-Menahem and Singh 1981) describing each anelastic deformation mode (identified by the index $\nu = 1$ for dilatations and $\nu = 2$ for distortions), whose (dimensionless) complex moduli can be expressed as

$$M_\nu(\omega) = \frac{\sqrt{Q_\nu^2+1} - 1 + {\rm i}\omega Q_\nu \tau_0}{\sqrt{Q_\nu^2+1} + 1 + {\rm i}\omega Q_\nu \tau_0}, \quad \nu = 1, 2, \tag{A17}$$

where ${\rm i} = \sqrt{-1}$, ω is the angular frequency, Q_ν are attenuation parameters, and τ_0 is a relaxation time (see Appendix C). The quality factor associated with each modulus is equal to the real part of M_ν divided by its imaginary part. At $\omega_0 = 1/\tau_0$, the associated quality factor curve has its highest value Q_ν. The high-frequency limit corresponds to the elastic case with $M_\nu \to 1$.

The unrelaxed wet-rock moduli of the porous medium are generalized to complex and frequency-dependent moduli, $K_{\rm c}$ and $\mu_{\rm c}$. We obtain

$$K_{\rm c} = \bar{\rho}\left(V_{\rm P}^2 - (4/3)V_{\rm S}^2\right) M_1 \quad \text{and} \quad \mu_{\rm c} = \bar{\rho} V_{\rm S}^2 M_2. \tag{A18}$$

A.4 Seismic model for the ice sheet

The anisotropic model for the ice sheet is that of transverse isotropy with a vertical symmetry axis. Pure ice is transversely isotropic, with the following elastic constants as a function of temperature (Angenheister 1982):

$$c_{IJ} = A_0 + A_1 T + A_2 T^2, \tag{A19}$$

where T is given in °C, and A_0, A_1 and A_2 are given in Table 2. We assume that c_{33} (associated with the vertical P-wave velocity) is less than c_{11} (associated with the horizontal P-wave velocity), contrary to the convention in Angenheister (1982), which depends on the orientation of the sample in the laboratory experiments. The inequality $c_{33} < c_{11}$ reflects the fact that the stress associated with the vertical compaction is greater than the horizontal stress.

The anisotropy parameters relevant to PS propagation are given by (Thomsen 1986)

$$\epsilon = \frac{c_{11} - c_{33}}{2c_{33}},$$

$$\delta = \frac{(c_{13} + c_{55})^2 - (c_{33} - c_{55})^2}{2c_{33}(c_{33} - c_{55})}. \tag{A20}$$

They quantify the anisotropy of the P-wave along the vertical and horizontal directions, and the deviation of the wave surface from an ellipsoid, respectively.

In order to introduce dissipation, we assume that the mean stress (i.e. the trace of the stress tensor) depends only on the dilatational complex modulus M_1. Moreover, the deviatoric stress components depend solely on the shear complex modulus, denoted by M_2. The complex stiffnesses for the transversely isotropic and viscoelastic medium are then given by (Carcione *et al.* 1998)

$$\begin{aligned} c^*_{I(I)} &= c_{I(I)} - \bar{D} + \bar{K} M_1 + c_{55} M_2, \quad I = 1, 2, 3, \\ c^*_{IJ} &= c_{IJ} - \bar{D} + \bar{K} M_1 + c_{55}(1 - M_2), \quad I, J = 1, 2, 3; \quad I \neq J, \\ c^*_{55} &= c_{55} M_2, \end{aligned} \tag{A21}$$

where M_ν is given in (A17), K is given in (C6) and $\bar{D} = \bar{K} + c_{55}$.

A.5 Seismic model for fluid-filled porous ice

We consider that ice saturated with a fluid (air or mud in this case) consists of fluid bubbles embedded in an ice matrix. The complex stiffness of this composite medium can be calculated by using the model developed by Kuster and Toksöz (1974) for spherical inclusions, when the inclusion concentration is low, as is the case in accreted ice. If s is the fluid saturation, the high-frequency compression and shear moduli are obtained from

$$\frac{K}{K_{\rm i}} = \frac{1 + [4\mu_{\rm i}(K_{\rm f} - K_{\rm i})/(3K_{\rm f} + 4\mu_{\rm i})K_{\rm i}]s}{1 - [3(K_{\rm f} - K_{\rm i})/(3K_{\rm f} + 4\mu_{\rm i})]s} \tag{A22}$$

and

$$\frac{\mu}{\mu_{\rm i}} = \frac{(1-s)(9K_{\rm i} + 8\mu_{\rm i})}{9K_{\rm i} + 8\mu_{\rm i} + s(6K_{\rm i} + 12\mu_{\rm i})}, \tag{A23}$$

where $K_{\rm i}$ and $K_{\rm f}$ are the ice and fluid compression moduli, and $\mu_{\rm i}$ is the shear modulus of the ice. The high-frequency or unrelaxed wave velocities are then given by

$$V_{\rm P} = \left(\frac{K + 4\mu/3}{\rho}\right)^{1/2} \text{and} \quad V_{\rm S} = \left(\frac{\mu}{\rho}\right)^{1/2}. \tag{A24}$$

The density of the composite is given by

$$\rho = (1 - s)\rho_{\rm i} + s\rho_{\rm f}, \tag{A25}$$

where ρ_i and ρ_f are the ice and fluid densities, respectively.

The complex moduli of the fluid-filled porous ice are then given by

$$K_c = KM_1 \quad \text{and} \quad \mu_c = \mu M_2, \tag{A26}$$

where M_1 and M_2 are given in (A17).

APPENDIX B

Reflection coefficients

B.1 Ice/water interface

The AVA analysis of the interface between accreted ice and water requires the solution of the reflection–refraction problem between an isotropic-viscoelastic medium (accreted ice) and a lossless acoustic medium (water). We use the methodology and the notation given in Carcione (1997), and consider single-phase media. This problem, solved using Biot's theory, can be found in Yew and Weng (1987), but the differences with the single-phase case are not significant from a practical point of view (Gurevich 1996; Carcione 1998). We assume an incident homogeneous P-wave, for which the propagation direction coincides with the attenuation direction.

A general plane-wave solution for the particle-velocity field $\mathbf{v} = (v_x, v_z)$ is

$$\mathbf{v} = \mathrm{i}\omega\, \mathbf{U} \exp\left[\mathrm{i}\omega(t - s_x x - s_z z)\right], \tag{B1}$$

where s_x and s_z are the components of the complex slowness vector, t is the time variable and $\mathbf{U}$ is a complex vector. For homogeneous waves, the directions of propagation and attenuation coincide and

$$s_x = \sin\theta / v_{\mathrm{P}_1}, \tag{B2}$$

where θ is the incidence propagation angle, measured with respect to the z-axis, and v_{P_1} is the complex velocity, in this case, the complex P-wave velocity of accreted ice, given by

$$v_{\mathrm{P}_1} = \left(\frac{K_c + 4\mu_c/3}{\rho}\right)^{1/2}, \tag{B3}$$

where K_c and μ_c are given in (A26). We denote the complex shear-wave velocity of accreted ice by v_{S_1} and the real valued P-wave velocity in water by v_{P_2}.

The upper viscoelastic medium is denoted by subscript 1 and the acoustic medium by subscript 2. The symbol P indicates the compressional wave in the fluid or the P-wave in the upper layer, and S denotes the S-wave in this medium. Moreover, the subscripts I, R and T denote the incident, reflected and transmitted waves. Using symmetry properties to define the polarization of the reflected waves and using the fact that Snell's law implies the continuity of the horizontal slowness s_x, the particle velocities for a P-wave incident from the upper medium are given by

$$\mathbf{v}_1 = \mathbf{v}_{\mathrm{P_I}} + \mathbf{v}_{\mathrm{P_R}} + \mathbf{v}_{\mathrm{S_R}}, \tag{B4}$$

$$\mathbf{v}_2 = \mathbf{v}_{\mathrm{P_T}}, \tag{B5}$$

where

$$\mathbf{v}_{\mathrm{P_I}} = \mathrm{i}\omega \left(\beta_{\mathrm{P}_1}, \gamma_{\mathrm{P}_1}\right)^{\top} \exp\left[\mathrm{i}\omega\left(t - s_x x - s_{z\mathrm{P}_1} z\right)\right], \tag{B6}$$

$$\mathbf{v}_{\mathrm{P_R}} = \mathrm{i}\omega \mathrm{R_{PP}} \left(\beta_{\mathrm{P}_1}, -\gamma_{\mathrm{P}_1}\right)^{\top} \exp\left[\mathrm{i}\omega\left(t - s_x x + s_{z\mathrm{P}_1} z\right)\right], \tag{B7}$$

$$\mathbf{v}_{\mathrm{S_R}} = \mathrm{i}\omega \mathrm{R_{PS}} \left(\beta_{\mathrm{S}_1}, -\gamma_{\mathrm{S}_1}\right)^{\top} \exp\left[\mathrm{i}\omega\left(t - s_x x + s_{z\mathrm{S}_1} z\right)\right], \tag{B8}$$

$$\mathbf{v}_{\mathrm{P_T}} = \mathrm{i}\omega T_{\mathrm{PP}} \left(\beta_{\mathrm{P}_2}, \gamma_{\mathrm{P}_2}\right)^{\top} \exp\left[\mathrm{i}\omega\left(t - s_x x - s_{z\mathrm{P}_2} z\right)\right]. \tag{B9}$$

The slownesses and vertical slowness components are

$$\begin{aligned} s_{\mathrm{P}_1} &= 1/v_{\mathrm{P}_1}, \quad s_{z\mathrm{P}_1} = \text{p.v.}\left(s_{\mathrm{P}_1}^2 - s_x^2\right)^{1/2}, \\ s_{\mathrm{S}_1} &= 1/v_{\mathrm{S}_1}, \quad s_{z\mathrm{S}_1} = \text{p.v.}\left(s_{\mathrm{S}_1}^2 - s_x^2\right)^{1/2}, \\ s_{\mathrm{P}_2} &= 1/v_{\mathrm{P}_2}, \quad s_{z\mathrm{P}_2} = \left(s_{\mathrm{P}_2}^2 - s_x^2\right)^{1/2}, \end{aligned} \tag{B10}$$

where p.v. denotes the principal value, and the polarizations are

$$\beta_{\mathrm{P}_m} = \frac{s_x}{s_{\mathrm{P}_m}}, \quad \gamma_{\mathrm{P}_m} = \frac{s_{z\mathrm{P}_m}}{s_{\mathrm{P}_m}}, \quad \beta_{\mathrm{S}_1} = \frac{s_{z\mathrm{S}_1}}{s_{\mathrm{S}_1}}, \quad \gamma_{\mathrm{S}_1} = -\frac{s_x}{s_{\mathrm{S}_1}}, \quad m = 1, 2. \tag{B11}$$

The boundary conditions require continuity of

$$v_z, \quad \sigma_{zz}, \quad \text{and} \quad \sigma_{xz}(=0). \tag{B12}$$

Using the isotropic version of the stress components (C4) and (C5), we find that the boundary conditions generate the following matrix equation for the reflection and transmission coefficients:

$$\begin{pmatrix} \gamma_{\mathrm{P}_1} & \gamma_{\mathrm{S}_1} & \gamma_{\mathrm{P}_2} \\ Z_{\mathrm{P}_1} & Z_{\mathrm{S}_1} & -Z_{\mathrm{P}_2} \\ W_{\mathrm{P}_1} & W_{\mathrm{S}_1} & 0 \end{pmatrix} \begin{pmatrix} R_{\mathrm{PP}} \\ R_{\mathrm{PS}} \\ T_{\mathrm{PP}} \end{pmatrix} = \begin{pmatrix} \gamma_{\mathrm{P}_1} \\ -Z_{\mathrm{P}_1} \\ W_{\mathrm{P}_1} \end{pmatrix}, \tag{B13}$$

where

$$\begin{aligned} Z_m &= \rho_1 v_{\mathrm{P}_1}^2 \gamma_m s_{zm} + \rho_1 \left(v_{\mathrm{P}_1}^2 - 2v_{\mathrm{S}_1}^2\right) \beta_m s_x, \\ W_m &= \rho_1 v_{\mathrm{S}_1}^2 (\beta_m s_{zm} + \gamma_m s_x) \end{aligned} \tag{B14}$$

for the upper medium, where subscript m is either P_1 or S_1, and

$$Z_{\mathrm{P}_2} = \rho_2 v_{\mathrm{P}_2}^2 \left(\gamma_{\mathrm{P}_2} s_{z\mathrm{P}_2} + \beta_{\mathrm{P}_2} s_x\right), \quad W_{\mathrm{P}_2} = 0 \tag{B15}$$

for the fluid.

The steps to compute the reflection and refraction coefficients are the following:

1 The horizontal slowness s_x is the independent parameter. It is the same for all the waves (viscoelastic Snell's law). For an incident homogeneous wave, the independent variable becomes the angle of incidence θ, and s_x is obtained from (B2).

2 Compute $s_{z\mathrm{P}_1}$, $s_{z\mathrm{P}_2}$ and $s_{z\mathrm{S}_1}$ using (B10). For an incident homogeneous wave, $s_{z\mathrm{P}_1}$ can be calculated either from (B10) or from (B2).

3 Compute β_{P_1}, β_{P_2}, β_{S_1}, γ_{P_1}, γ_{P_2} and γ_{S_1} using (B11).

4 Compute Z_{P_1}, Z_{P_2}, Z_{S_1}, W_{P_1} and W_{S_1} using (B14) and (B15).

5 Compute the reflection and transmission coefficients by solving (B13).

B.2 Water/sediment interface

In this case, the fluid is denoted by the subscript 1 and the lower layer by the subscript 2. The particle velocities for a P-wave incident from the fluid are given by

$$\mathbf{v}_1 = \mathbf{v}_{\mathrm{P_I}} + \mathbf{v}_{\mathrm{P_R}}, \tag{B16}$$

$$\mathbf{v}_2 = \mathbf{v}_{\mathrm{P_T}} + \mathbf{v}_{\mathrm{S_T}}, \tag{B17}$$

where

$$\mathbf{v}_{\mathrm{P_I}} = \mathrm{i}\omega \left(\beta_{\mathrm{P}_1}, \gamma_{\mathrm{P}_1}\right)^\top \exp\left[\mathrm{i}\omega \left(t - s_x x - s_{z\mathrm{P}_1} z\right)\right], \tag{B18}$$

$$\mathbf{v}_{\mathrm{P_R}} = \mathrm{i}\omega R_{\mathrm{PP}} \left(\beta_{\mathrm{P}_1}, -\gamma_{\mathrm{P}_1}\right)^\top \exp\left[\mathrm{i}\omega \left(t - s_x x + s_{z\mathrm{P}_1} z\right)\right], \tag{B19}$$

$$\mathbf{v}_{\mathrm{P_T}} = \mathrm{i}\omega T_{\mathrm{PP}} \left(\beta_{\mathrm{P}_2}, \gamma_{\mathrm{P}_2}\right)^\top \exp\left[\mathrm{i}\omega \left(t - s_x x - s_{z\mathrm{P}_2} z\right)\right], \tag{B20}$$

$$\mathbf{v}_{\mathrm{S_T}} = \mathrm{i}\omega T_{\mathrm{PS}} \left(\beta_{\mathrm{S}_2}, \gamma_{\mathrm{S}_2}\right)^\top \exp\left[\mathrm{i}\omega \left(t - s_x x - s_{z\mathrm{S}_2} z\right)\right]. \tag{B21}$$

The boundary conditions (B12) generate the following matrix equation for the reflection and transmission coefficients:

$$\begin{pmatrix} \gamma_{\mathrm{P}_1} & \gamma_{\mathrm{P}_2} & \gamma_{\mathrm{S}_2} \\ Z_{\mathrm{P}_1} & -Z_{\mathrm{P}_2} & -Z_{\mathrm{S}_2} \\ 0 & W_{\mathrm{P}_2} & W_{\mathrm{S}_2} \end{pmatrix} \begin{pmatrix} R_{\mathrm{PP}} \\ T_{\mathrm{PP}} \\ T_{\mathrm{PS}} \end{pmatrix} = \begin{pmatrix} \gamma_{\mathrm{P}_1} \\ -Z_{\mathrm{P}_1} \\ 0 \end{pmatrix}, \tag{B22}$$

where β_{P_1}, β_{P_2}, β_{S_2}, γ_{P_1}, γ_{P_2}, γ_{S_2}, Z_{P_1}, Z_{P_2}, Z_{S_2}, W_{P_2} and W_{S_2} are obtained from (B11), (B14) and (B15), with the material indices interchanged ($1 \rightarrow 2$ and $2 \rightarrow 1$).

APPENDIX C

2D qP-qSV modelling equations

We consider the two-dimensional velocity–stress equations for propagation in the (x, z)-plane of a transversely isotropic medium. The constitutive equations assign one relaxation mechanism for dilatational anelastic deformations ($\nu = 1$) and one relaxation mechanism for shear anelastic deformations ($\nu = 2$). The constitutive equations satisfy the condition that the mean stress depends only on the dilatational relaxation function in any coordinate system (the trace of the stress tensor should be invariant under coordinate transformations). Moreover, the deviatoric stresses depend solely on the shear relaxation function.

The equations governing wave propagation can be expressed by

1 Newton's equations:

$$\partial_x \sigma_{xx} + \partial_z \sigma_{xz} = \rho \partial_t v_x + f_x, \tag{C1}$$

$$\partial_x \sigma_{xz} + \partial_z \sigma_{zz} = \rho \partial_t v_z + f_z, \tag{C2}$$

where v, σ and f denote particle velocity, stress and body force, respectively, ρ is the density, and ∂_a denotes the partial derivative with respect to a.

2 Constitutive equations:

$$\partial_t \sigma_{xx} = c_{11}\partial_x v_x + c_{13}\partial_z v_z + \bar{K}\epsilon_1 + 2c_{55}\epsilon_2 + f_{xx}, \tag{C3}$$

$$\partial_t \sigma_{zz} = c_{13}\partial_x v_x + c_{33}\partial_z v_z + \bar{K}\epsilon_1 - 2c_{55}\epsilon_2 + f_{zz}, \tag{C4}$$

$$\partial_t \sigma_{xz} = c_{55}[(\partial_z v_x + \partial_x v_z) + \epsilon_3] + f_{xz}, \tag{C5}$$

where ϵ_1, ϵ_2 and ϵ_3 are memory variables, and

$$\bar{K} = \frac{1}{2}(c_{11} + c_{33}) - c_{55}. \tag{C6}$$

3 Memory variable equations:

$$\partial_t \epsilon_1 = \frac{1}{\tau_\sigma^{(1)}}\left[\left(\frac{\tau_\sigma^{(1)}}{\tau_\epsilon^{(1)}} - 1\right)(\partial_x v_x + \partial_z v_z) - \epsilon_1\right], \tag{C7}$$

$$\partial_t \epsilon_2 = \frac{1}{2\tau_\sigma^{(2)}}\left[\left(\frac{\tau_\sigma^{(2)}}{\tau_\epsilon^{(2)}} - 1\right)(\partial_x v_x - \partial_z v_z) - 2\epsilon_2\right], \tag{C8}$$

$$\partial_t \epsilon_3 = \frac{1}{\tau_\sigma^{(2)}}\left[\left(\frac{\tau_\sigma^{(2)}}{\tau_\epsilon^{(2)}} - 1\right)(\partial_z v_x + \partial_x v_z) - \epsilon_3\right], \tag{C9}$$

where $\tau_\sigma^{(\nu)}$ and $\tau_\epsilon^{(\nu)}$ are material relaxation times. These can be expressed as

$$\tau_\epsilon^{(\nu)} = \frac{\tau_0}{Q_\nu}\left[\sqrt{Q_\nu^2+1}+1\right] \text{ and } \tau_\sigma^{(\nu)} = \frac{\tau_0}{Q_\nu}\left[\sqrt{Q_\nu^2+1}-1\right], \tag{C10}$$

where τ_0 is a relaxation time such that $1/\tau_0$ is the centre frequency of the relaxation peak and Q_ν are the minimum quality factors (see Appendix A.3). Superscripts and subscripts $\nu = 1$ and $\nu = 2$ correspond to dilatational and shear deformations, respectively.

Equations (C1)–(C9) are modified and simplified versions of the differential equations given in Carcione (1997), which avoid the explicit introduction of the low-frequency, relaxed elasticity constants. The difference resides in the definition of the memory variables.